

Reply to Reviewer #1

Thank you very much for your careful review and valuable comments. Your comments and suggestions lead to a great improvement of our manuscript. Our point-by-point responses are as follows:

This study examined the role of inner eyewall structure in the formation of a secondary eyewall by performing two WRF simulations of (realistic or idealized unknown) tropical cyclones (TCs) with different horizontal grid spacings. The simulation with secondary eyewall formation (SEF) has stronger and deeper eyewall updrafts that produce more hydrometers falling out of anvil clouds outside the eyewall. The associated diabatic cooling helps induce a descending inflow beneath the outflow layer that is argued to contribute to the formation of a moat. In contrast, the simulation without SEF does not show the descending inflow and moat. The authors then emphasized the importance of accurately simulating the structure of the eyewall in the SEF.

I would like to appreciate the substantial efforts the authors made to diagnose the mechanism responsible for the formation of descending inflows outside the primary eyewall. However, after going through the paper, I fail to locate any solid evidence that can support the statement that the descending inflow outside the eyewall contributes to the SEF. The literature review is insufficient, and thus key findings from this study are mostly facts we have learned from previous studies. The model design is not clear and the experiment design with different horizontal grid spacings needs to be justified. The writing suffers from numerous grammatical errors. In some instances the grammatical issues were so severe that I could not discern the meaning of the authors. If the revised manuscript is not substantially improved to address these issues, then I will recommend rejection.

Reply: Thank you very much for your comments. We would like to provide our detailed responses to each comment below.

General comments:

1. The take-home message of this study is compared to non-SEF TCs SEF TCs have stronger intensity, and stronger upper-level inflows that descend into the boundary layer and contribute to a formation of moat. Is this a novel finding? A statistical analysis of Western North Pacific typhoons (Kuo et al. 2009) has shown that major typhoons are more likely to undergo SEF than weaker typhoons (see their Fig. 4). Additionally, an existed debate is the relative importance between strong strain flows that shear apart or suppress convection (Kossin et al. 2000; Rozoff et al. 2006) and subsidence, a component of the secondary circulation; the latter is argued to be the dominant factor by Wang et al. (2008). The related discussion is missing in the literature review. The inflow layer beneath the outflow layer for SEF TCs can be a response to momentum forcing, radiation, and many other factors, while authors only diagnosed the contribution of diabatic heating. Differences in TC structure and inflow strength between the two experiments are largely attributable to differences in TC intensity. I don't understand the motive of revisiting these processes. Most importantly, please provide solid evidence to prove the descending inflow contributes to the SEF.

Reply:

The take-home message: As we know, the SEF mainly occurs in major hurricanes, which usually have strong eyewall updrafts and the higher-level anvil. So far, to our knowledge, few studies have demonstrated the influence of the inner eyewall structure, although some studies implied it. In this study, our objective is to understand whether the inner eyewall structure affects the formation of the moat since the moat formation is also a key process to the SEF.

In this study, we find that (Fig. R1.1, replace Fig. 12), in response to the diabatic warming in the eyewall with strong updrafts and large quantities of hydrometeors, an upper-level dry inflow can occur below the anvil. The drying effects caused by the inflow enhance diabatic cooling below the anvil, which causes negative buoyancy and prompts the subsidence. As feedback, the diabatic cooling with subsidence further enhances the upper-level inflow. Therefore, the moat forms

with subsidence, which separates the inner eyewall from the spiral rainbands that intensify and extend symmetrically into a secondary eyewall.

The strain flows VS. subsidence in the moat formation: The related discussions of the other possible reasons for the moat formation have been added in the introduction as follows, and the related literature is cited.

“Some studies also examined the formation of the moat, by which the spiral rainband is separated from the inner eyewall with a chance to become a secondary eyewall and its importance in the SEF. Willoughby et al. (1982) suggested that the moat was generated due to the evaporative cooling of precipitation falling from the cumulus anvil, which is also suggested by Dodge et al. (1999), Wang (2008), and Zhu and Zhu (2015). In our previous study based on a numerical modeling simulation (Qin et al., 2021), we demonstrated that the moat subsidence is mainly caused by the negative buoyancy resulting from the cooling from sublimation, melting, and evaporation processes of hydrometeors from the cumulus eyewall and the related well-developed anvil. Although the subsidence plays an important role in the moat formation, there are additional dynamics that may play a role in the moat formation. Kossin et al. (2000) provided that straining zones are possible reasons for the formation of the moat. The moat formed in the rapid filamentation zone of about 30-km wide annular region outside the radius of the maximum tangential wind, where deep convection was distorted or suppressed. This possible mechanism leading to the formation of a moat is also supported by Rozoff et al. (2006) and Wang (2008). The relative importance between the rapid filamentation zone and subsidence in the formation of the moat is still unclear.”

We also examined the role of filamentation time in the moat formation (Fig. R1.2). The moat occurs in a region of strain-dominated flow (radii between 30 km and 50 km) in CTL, which is consistent with other studies (Kossin et al. 2000; Rozoff et al. 2006; Wang 2008). However, the rapid filamentation zones from 30-km to 50-km radii are also found in NSEF. Thus, although the strong strain-flow zones are important to the moat formation, they are not the crucial factor here.

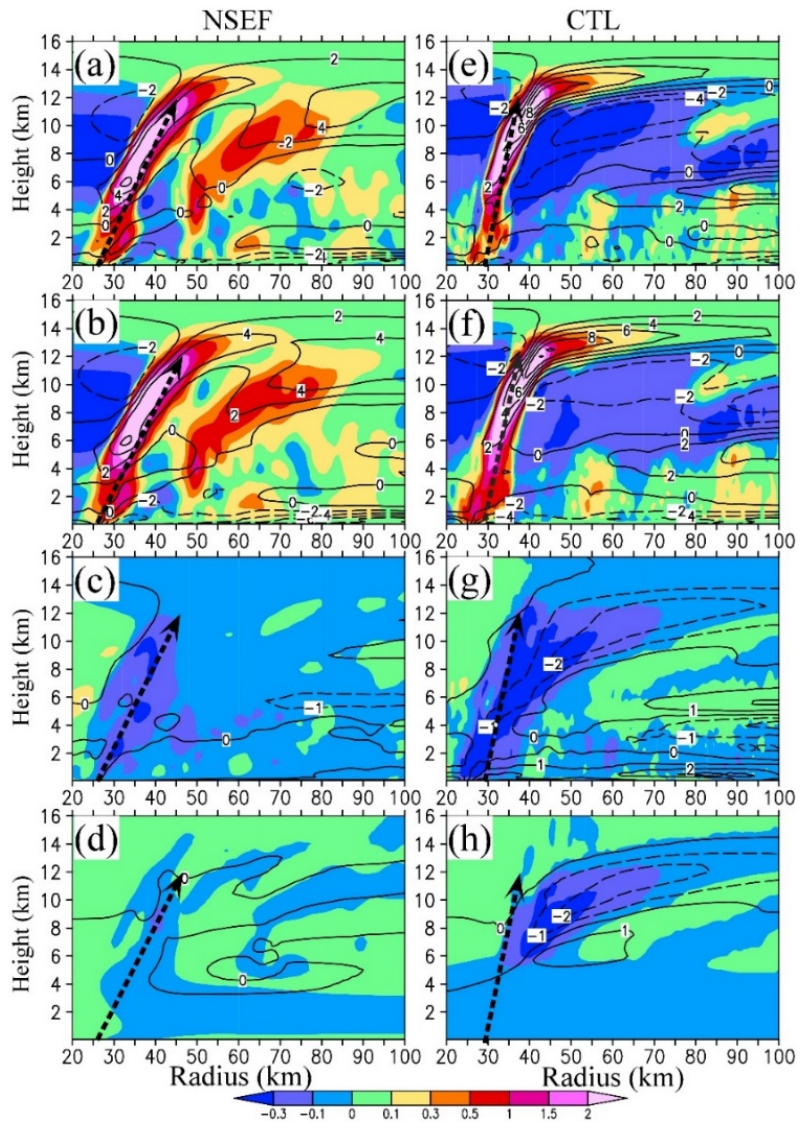


Figure. R1.1 Radius-height cross-sections of the upshear-right quadrant-mean vertical (shaded, m s^{-1}) and radial motion (contours, m s^{-1}) forced by the (a, e) diabatic heating, (b, f) diabatic warming, (c, g) diabatic cooling, (d, h) sublimation cooling at 30 h for (a-d) NSEF and (c-h) CTL. Note that the radial wind is at 2 m s^{-1} intervals in (a) and (e), and 1 m s^{-1} intervals in others. The white dashed lines with 0.5 m s^{-1} vertical motion indicate the eyewall convection region. The black dashed arrows denote the eyewall. The new Fig. 12 in the revision.

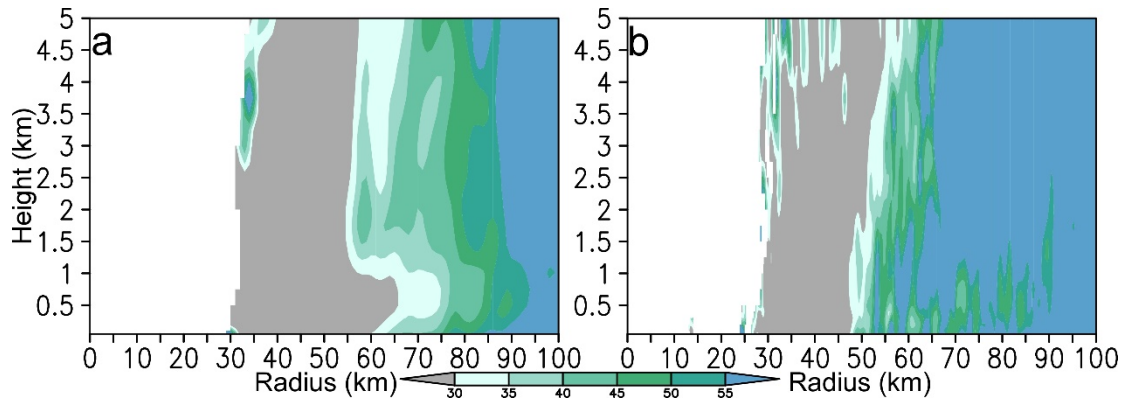


Figure. R1.2 Radius-height cross-section of the azimuthal-mean filamentation time (min) averaged in 6 h between 32 and 38 h of (a) NSEF and (b) CTL.

The upper-level inflows: We examined the momentum forcing, the unbalanced processes, the TC intensity, and the large-scale VWS that may affect the strength of the upper-level inflows beneath the outflow layer for our simulations.

For the momentum forcing, however, in the present model output, we do not have the output of the diffusion (or the momentum forcing term), and the residual term cannot be treated as the momentum forcing term since the errors are relatively large when the momentum budget is calculated using the 1-h output data in the present model. We carefully compare the SEE-diagnosed results to the model results using the 5-min output model data related to the other case in Fig. R1.3. In general, SEE-diagnosed fields capture well the secondary circulation above the boundary layer and below the main outflow layer, which is consistent with other studies (e.g., Bui et al. 2009; Zhu and Zhu 2014; Wang et al. 2020). For Wilma, the eyewall heating accounts for a large part of the radial and vertical wind above the boundary layer, while the momentum forcing did less. Wang et al. (2020) also proposed that “*the secondary circulation associated with the diabatic heating dominates that associated with the momentum forcing*”. Thus, *we believe that the momentum forcing has a small impact on the secondary circulation above the boundary layer compared to the heating forcing.*

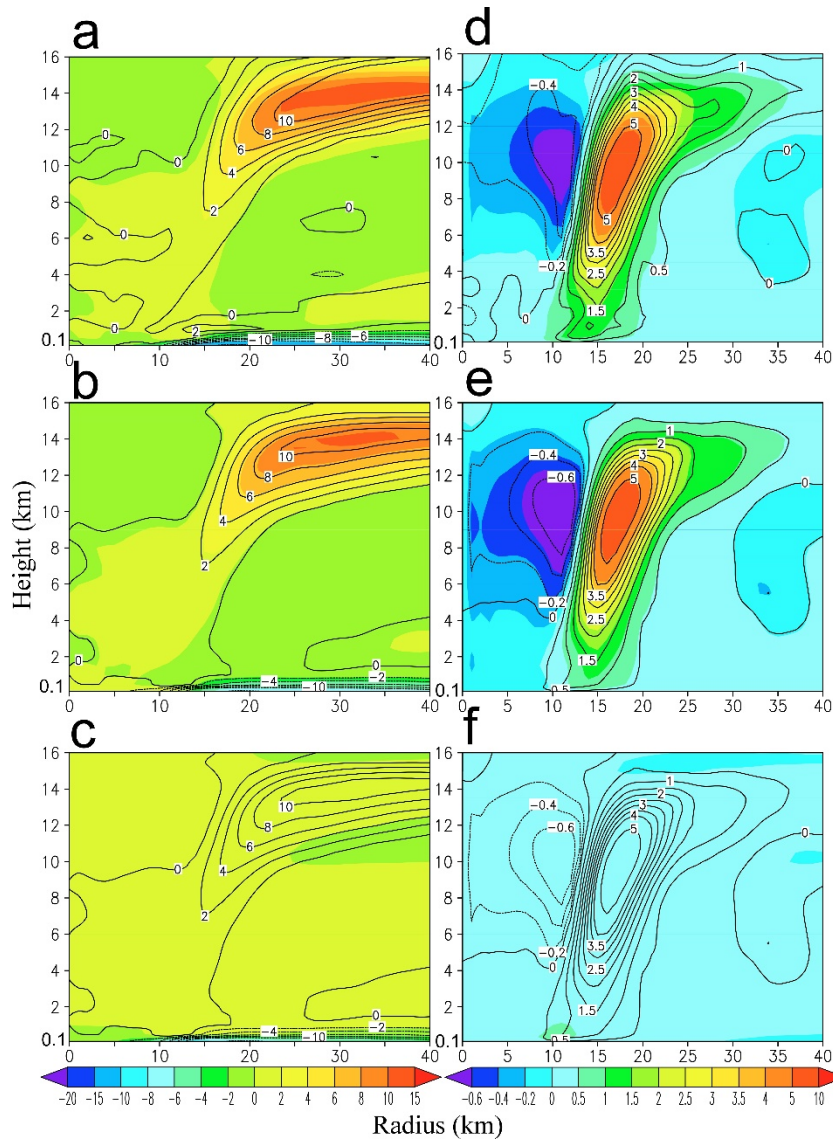


Figure. R1.3 Radius-height cross-sections of the azimuthal-mean (a, b, c) radial and (d, e, f) vertical winds (m s^{-1}) at 1800 UTC 18 October 2005. Panels (a) and (d) compare the model-output (contour) to SEE-diagnosed results (shaded). Contours in (b, c, e, f) are SEE-diagnosed results. Shading in (b) and (e) shows SEE-diagnosed results forced only by diabatic heating; while shading in (c) and (f) indicates SEE-diagnosed results forced only by momentum.

For unbalanced force: Previous studies have confirmed that the inward agradiant force determines the inflows (Montgomery et al. 2020; Wang et al. 2020). Focusing on the upper-level inflows below the outflow layer, we examine the agradiant force in Fig. R1.4 in terms of the azimuthal and the quadrantal mean to understand the upper-level inflows. There is gradient wind imbalance especially within the boundary layer, along the slantwise eyewall, and within the outflow layer.

Inward force persists and will accelerate the parcels inwards below the outflow layer and outside the eyewall, which is more significant in the quadrant-mean results, indicating that the upper-level inflow is associated with imbalanced forces. We highlighted the importance of the agradient force in the acceleration of the inflows in our revision, and we also believed that both the balanced and unbalanced processes determine the evolution of the inflow. In addition, further investigation is needed to understand how the pressure field adjusts to the diabatic heating/cooling force in the layer with inflows.

Thank you for the important literature you recommended, and we referred to those studies (Montgomery et al. 2020; Wang et al. 2020; Wang et al. 2021), and related discussions were added in the revision:

Previous studies indicated that the agradient force determines the inflows in TCs (Montgomery et al. 2020; Wang et al. 2020; Wang et al. 2021). We also examine the agradient force (not shown here) and confirm that the upper-level inflow is associated with imbalanced forces. The inward force will accelerate the parcels inwards below the outflow layer, suggesting that both the balanced and unbalanced processes are important to the evolution of the upper-level inflow.

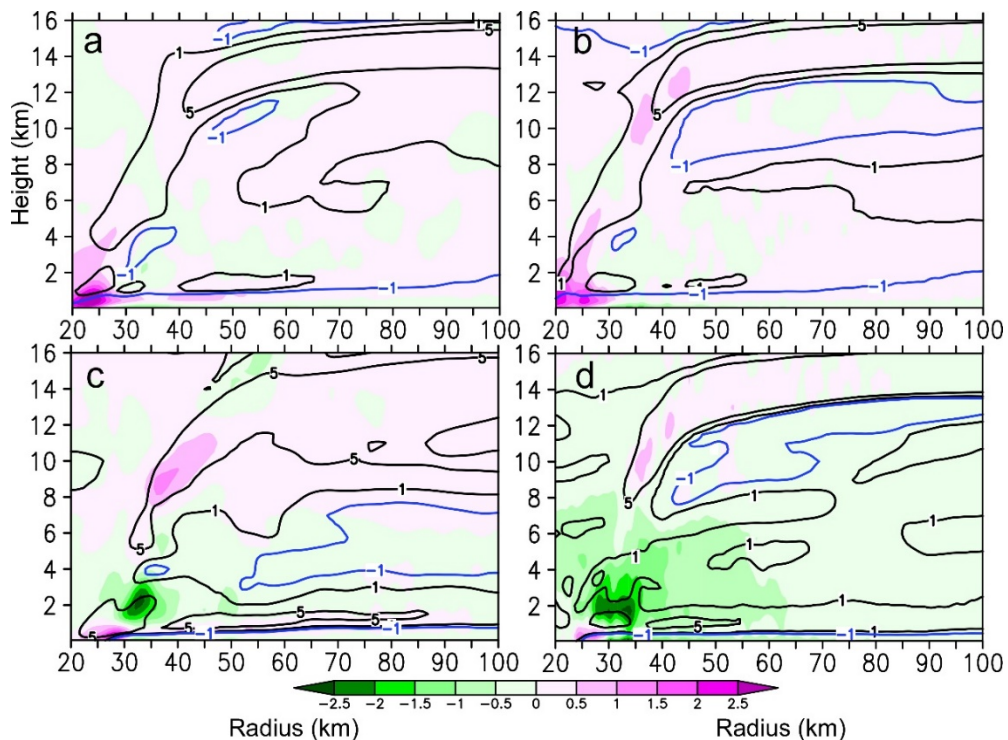


Figure. R1.4 Radius-height cross-sections of the (a, b) azimuthal-mean and (c, d) upshear-right quadrant-mean agradiant force (shaded, $10^{-2} \text{ m s}^{-1} \text{ s}^{-1}$) and the radial wind (outflows of 1 and 5 m s^{-1} in black lines and inflows of -1 m s^{-1} in blue lines) at 30 h for (a, c) NSEF and (b, d) CTL.

For the TC intensity: Differences in TC structure are largely attributable to differences in TC intensity, and the evolution of eyewall updrafts, diabatic heating, and hydrometeors with convection usually affect the change of TC intensity. The motivation of our study is to understand how the inner eyewall structure affects the formation of the moat since the mechanisms for the moat formation are still debated. Figure R1.5 examines the distribution of the solid hydrometeors in the two simulations. More solid hydrometeors occur at the upper-level anvil in CTL depending on the stronger eyewall updrafts compared to the NSEF, which induce more cooling beneath the anvil at a higher level (Fig. R1.6). Any factor, like eyewall updrafts and *the radiation* that affect TC intensity, will affect the SEF.

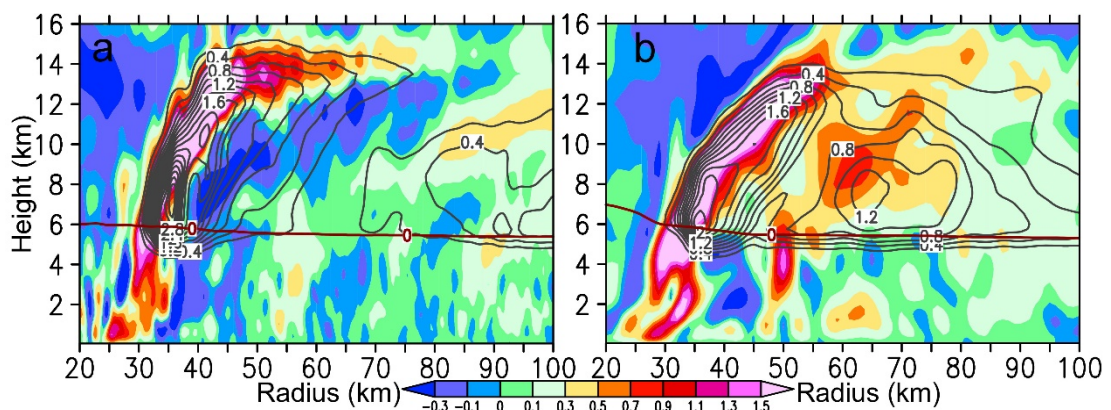


Figure. R1.5 Radius-height cross-sections of the upshear-right quadrant-mean vertical motion (shaded, m s^{-1}) and the solid hydrometeors (ice, snow, and graupel, contours, g kg^{-1}) at 30 h for (a) CTL and (b) NSEF. The red lines denote the melting level.

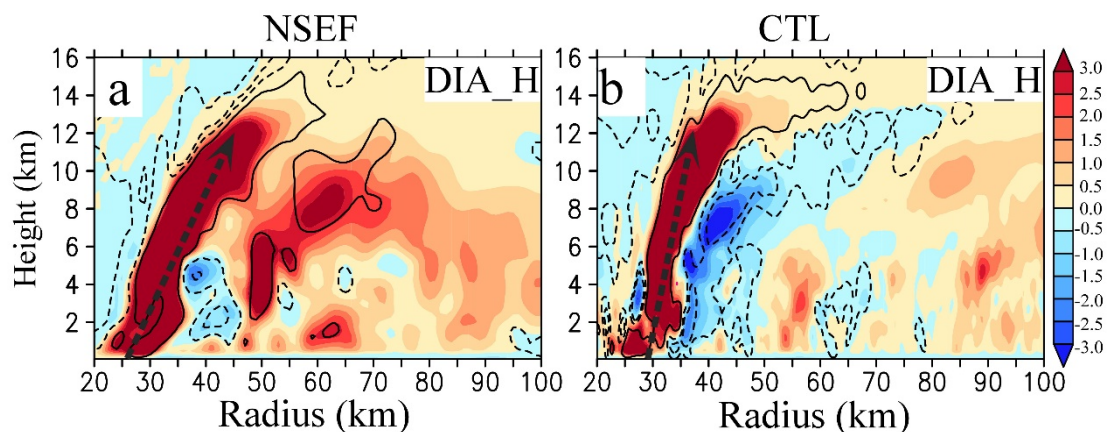


Figure. R1.6 Radius-height cross-sections of the quadrant-mean diabatic heating rate (shaded, 10^{-3} K s^{-1}) at 30 h for (a) NSEF and (b) CTL superimposed with the vertical motion (updraft, solid lines of 0.5 m s^{-1} ; downdrafts, dashed lines of -0.05 and -0.3 m s^{-1}). The black dashed arrows denote the eyewall.

For many other factors: For example, the large-scale vertical wind shear (Fig. R1.7) is similar for both the CTL and the NSEF since the large-scale condition used in the two simulations is the same. In fact, any factor that affects the inner-core structure and TC intensity are also important to the SEF.

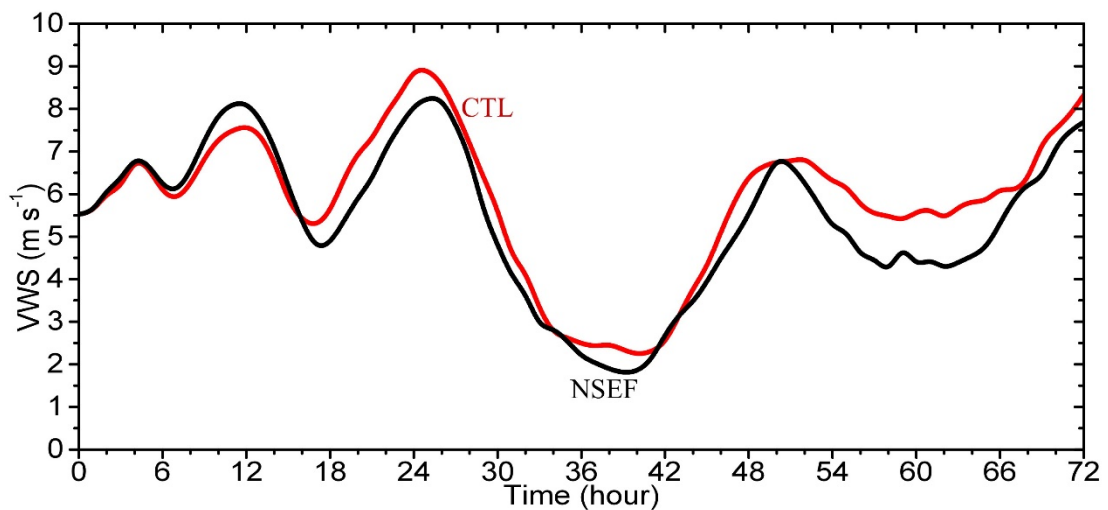


Figure. R1.7 Time series of the large-scale vertical wind shear (m s^{-1}) between 200 hPa and 850 hPa for NSEF (black) and CTL (red).

- The description for experiment design and model setup is not clear. Please inform readers whether these simulations use a realistic or an idealized TC. Reasons for performing simulations with different horizontal grid spacing are missing. Comparison of inner-core structure with different model grid spacing is not fair. The usage of a traditional PBL scheme at gray-zone resolutions (e.g., 333 m) is problematic. Given these issues, I would encourage the authors to perform ensemble simulations with 1-km horizontal grid spacing and compare the simulations with and without SEF.

Reply:

Descriptions for experiment design and model setup are added as follow:

The initial and lateral boundary conditions are derived from the environment of Typhoon Matsa (2005) using the National Centers for Environmental Prediction

(NCEP) Final (FNL) Operational Global Analysis dataset. The FNL data has a resolution of $1.0^\circ \times 1.0^\circ$ at 6-h intervals. Using the Lanczos method (Duchon 1979; Wu and Chen 2016; Qin et al. 2021), a 20-day low-pass filtering is conducted for the FNL data, which provides a large-scale condition to the simulations. Since the intensity of the TC in the FNL data is too weak, a warm-core vortex with the azimuthal-mean wind of about 29 m s^{-1} at a radius of 54 km after a 12-h spinup is put into the low-frequency background at 25.4°N , 123.0°E at the initial time (0000 UTC 5 August 2005). The method of the initialization follows Wang (2007) and any asymmetric flow component in the TC environment was still retained. Together with the azimuthal-mean vortex, the maximum 10-m sustained wind speed of the initial vortex used in this simulation is about 35 m s^{-1} . More model details can be found in Wu and Chen (2016) and Chen and Wu (2016).

Model grid spacing & LES & Ensemble simulations:

A 333-m resolution is at the gray zone. Therefore, we conducted a sensitivity using the large-eddy simulation (*LES*) instead of the PBL scheme on the 333-m domain. Figure R1.8 shows the horizontal distribution of the radar reflectivity using the LES. The SEF occurs but at a different time, depending on the changes of the inner-core structure and intensity by using the LES.

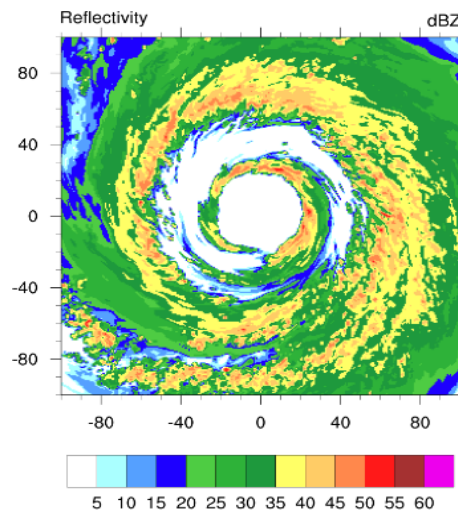


Figure. R1.8 Horizontal distributions of the radar reflectivity at the 5-km height at 42 h for the LES at 333-m grid spacing.

We conducted a *set of sensitivity experiments by changing the microphysics schemes with the same grid spacing of 333 m* since we do not have enough computation resources to do an ensemble due to the limited time. The microphysics schemes used are WSM6, WDM6, Thompson, and Lin.

Figure R1.9 shows that the SEF occurs in simulations with different microphysics schemes with a grid spacing of 333 m, while the timing of the SEF differs. In WDM6, the inner-eyewall convection does not develop vigorously from 20 h to 30 h. After 30 h, the inner-eyewall convection develops vigorously with strong eyewall updrafts shown in Fig. R1.9f. Thus, the SEF occurs around 48 h, which is 16-h later than that in WSM6. In Thompson and Lin, although the inner-eyewall updrafts are stronger than that in WSM6, the SEF occurs later than that in WSM6 due to different inner-eyewall structures. Figure R1.9 shows that the inner-eyewall expands from 24 h to 48 h, leading to the large-sized eyewall in Thompson and Lin compared to that in WSM6. Therefore, the SEF occurs earlier in WSM6 than that in Thompson and Lin. The sensitivity tests support our results that the SEF is sensitive to the inner-eyewall structure changes. And the SEF occurs when the eyewall updrafts are stronger, and the inner-eyewall convection becomes more compacted. We also conducted sensitivity experiments with 1-km horizontal grid spacing using different microphysics schemes (like WDM6 and Thompson). Figure R1.10 shows that no SEF occurs in simulations with different microphysics schemes with the grid spacing of 1 km.

Moreover, we think that the effects of grid spacing on turbulence and convection can be involved, to some extent, in the evolution of the eyewall convection. And the changes of the eyewall structures can be caused by any factor (like the different grid spacings, microphysics schemes, and initial vortex, etc.). The sensitivity tests support our results by showing that the SEF occurs when the eyewall updrafts are stronger, and the inner-eyewall convection is compacted, while understanding why eyewall structures differ to different factors is beyond the scope of our current study. Your suggestions have inspired us to do more research to understand why the inner-eyewall structure changes and to investigate the reliability

of the microphysics schemes on the SEF.

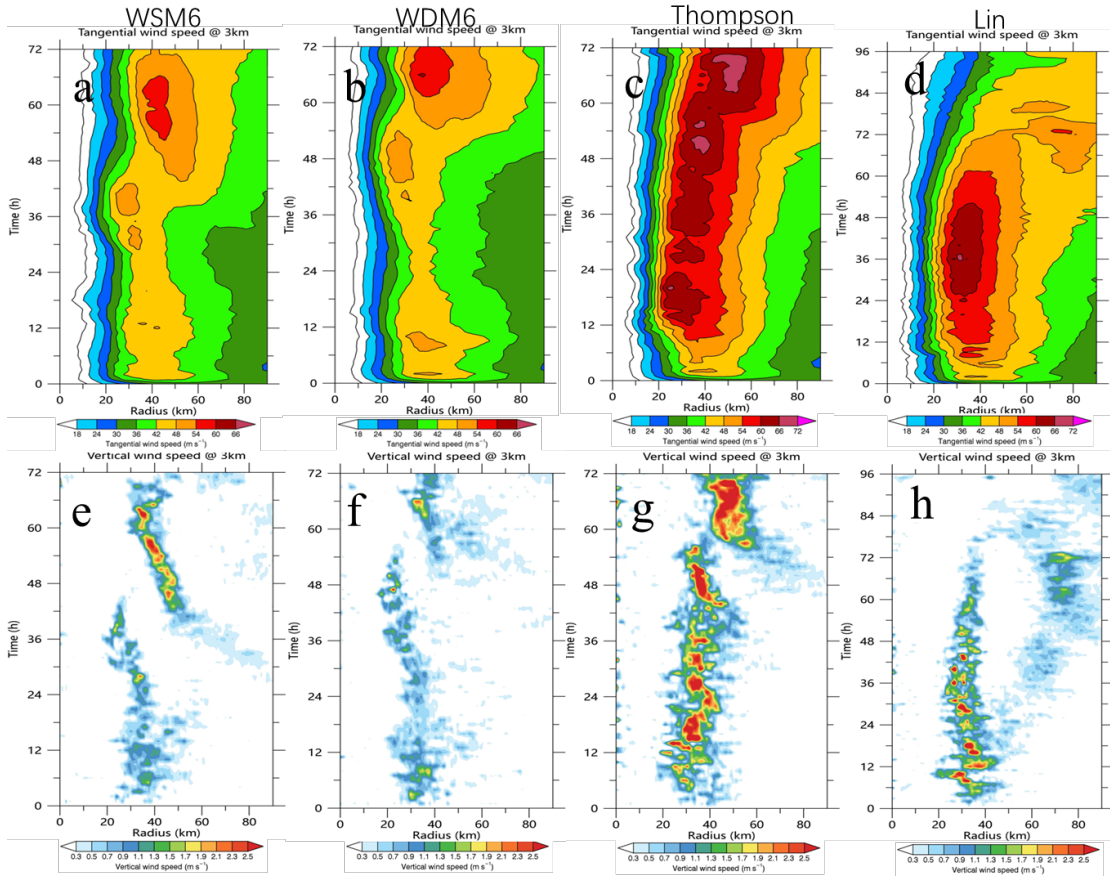


Figure R1.9 Radius-time cross-sections of the azimuthal mean (a-d) tangential wind (m s^{-1}) and (e-h) vertical motion (m s^{-1}) at $z = 3 \text{ km}$ for (a, e) WSM6, (b, f) WDM6, (c, g) Thompson, and (d, h) Lin with the horizontal grid spacing of 333 m.

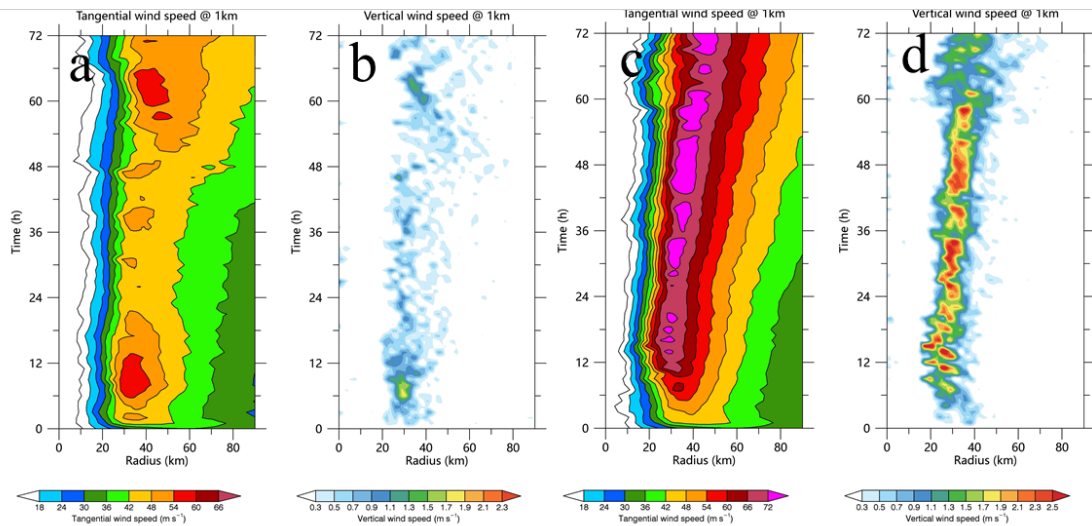


Figure R1.10 Radius-time cross-sections of the azimuthal mean (a, c) tangential wind (m s^{-1}) and (b, d) vertical motion (m s^{-1}) at $z = 1 \text{ km}$ for (a, b) WDM6 and (c, d) Thompson with the horizontal grid spacing of 1 km.

3. Different types of descending inflows have been documented in the literature,

including the one mentioned in this study, the one coming from the stratiform region outward of the outer rainband (Didlake et al. 2018), and the one coming from the upper levels and outward of the outer rainband (Dai et al. 2019). I would encourage the authors to discuss whether these processes are intrinsic to the SEF or they are the results of SEF based on their numerical simulations. The inflow layer beneath the outflow layer has been discussed in modeling studies (e.g., Wang et al. 2020, <https://doi.org/10.1002/qj.3856>). Under which situation would the inflow layer descend into the boundary layer and contribute to the moat and SEF formation? These descending inflows typically locate within a confined region around the TC center, and how do they contribute to the symmetrization of outer rainband during the SEF? These open questions need to be addressed to some extent to advance our understanding of SEF.

Reply: Thank you for the important literature you recommended. We have examined the processes related to inflows proposed by Didlake et al. (2018), Dai et al. (2019), and Wang et al. (2020) as follows:

We show the mean radial wind and vertical motion at large radii ($r \sim 200$ km) for both the upshear-right and the downshear-left (used by Didlake et al. 2018) quadrants in Fig. R1.11 to understand whether the processes mentioned by Didlake et al. (2018) and Dai et al. (2019) are intrinsic to the SEF in our cases. We found that:

i) The downshear-left quadrant of the two simulated TCs exhibited similar features, which is not the situation found by Didlake et al (2018), while notable and different features are found in the upshear-right quadrant for both the secondary circulation (Fig. R1.11) and the radar reflectivity (Fig. R1.12).

ii) the middle-level inflows associated with the outer rainbands travel radially inward but do not descend into the PBL in the two TCs for the upshear-right quadrant (Figs. R1.11a and R1.11b), which differ from the results found by Didlake et al. (2018) that the descending inflow can trigger convergence in the PBL and

upward acceleration in the region of SEF. Figure R1.14b shows that convergence occurs at radii from 80-120 km in the PBL in CTL, which forces upward acceleration and the SEF. However, this convergence is not related to the middle-level descending inflows from the outer rainbands mentioned by Didlake et al. (2018).

iii) no upper-level inflows are extending further outward to the outer rainbands (outside the radius of 100 km) in CTL with the SEF, indicating that the upper-level inflows in our cases are not coming from the outer outward of the outer rainband as mentioned by Dai et al. (2019).

iv) As our response to Comment 1, inward force occurs and accelerates the parcels inwards below the outflow layer and outside the eyewall, indicating that the upper-level inflow is associated with imbalanced forces (Fig. R1.4d), which is consistent with Wang et al. (2020). We highlighted the importance of the gradient force in the acceleration of the inflows in our revision, and we also believed that both the balanced and unbalanced processes are important to the evolution of inflows.

In summary, *those processes proposed by Didlake et al. (2018) and Dai et al. (2019) might not be intrinsic to the SEF at least for our simulated cases. The gradient force will accelerate the upper-level inflows as mentioned by Wang et al. (2020).* The upper-level inflows, which are largely forced by the diabatic warming in the eyewall and diabatic cooling below the outflow layer (Fig. R1.1e), extend from upper to middle levels before the SEF (from 30 h to 32 h, Fig. R1.13) and do not descend directly into the boundary layer. The upper-level dry inflows enhance diabatic cooling below the anvil, which causes negative buoyancy and prompts subsidence and moat formation. *The moat subsidence descends into the boundary layer and its related divergent flow meets with boundary inflows, leading to convergence at radii from 80 km to 120 km where the SEF (Figure R1.14). On the other hand, the middle-level moist inflows associated with the outer rainbands*

travel radially inward and also contribute to the SEF by intensifying the wind field through the inward transport of large angular momentum.

Following the azimuthal extension of the diabatic cooling under the anvil (Fig. 11 in the revision), the subsidence of the moat becomes symmetric. However, the upper-level inflow shows likely a wavenumber-1 pattern, which is not a reason for the symmetrization of the outer rainband. The old Fig. 14 was deleted and replaced by Fig. R1.15 showing the convergence at radii of 80-120 km below 1-km height. The notable feature for the SEF is the enhanced convergence within the boundary layer along with the azimuthal extension of the moat subsidence. The enhanced convergence forces convection and increases the axisymmetric tangential wind via the axisymmetric dynamical process with the large filamentation time (Terwey and Montgomery 2008). Figure R1.15 and their related discussions are added in section 5.3.

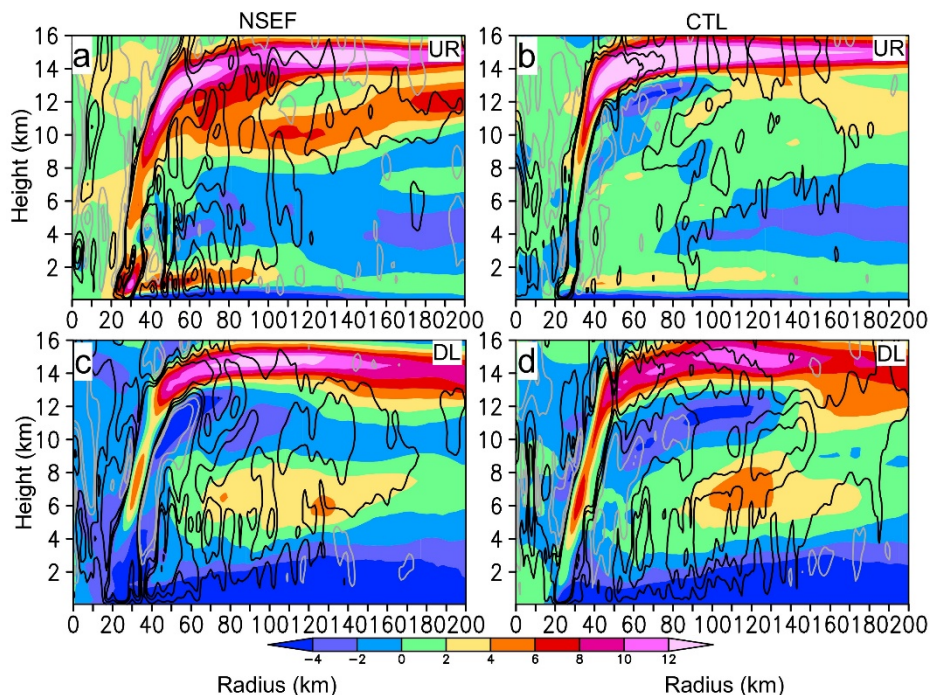


Figure. R1.11 Radius-height cross-sections of the quadrant-mean radial (shaded, m s^{-1}) and vertical wind (black lines of 0.1, 0.3, and 0.5 m s^{-1} ; gray lines of -0.1 and -0.3 m s^{-1}) for the (a, b) upshear-right and the (c, d) downshear-left quadrants at 30 h for (a, c) NSEF and (b, d) CTL.

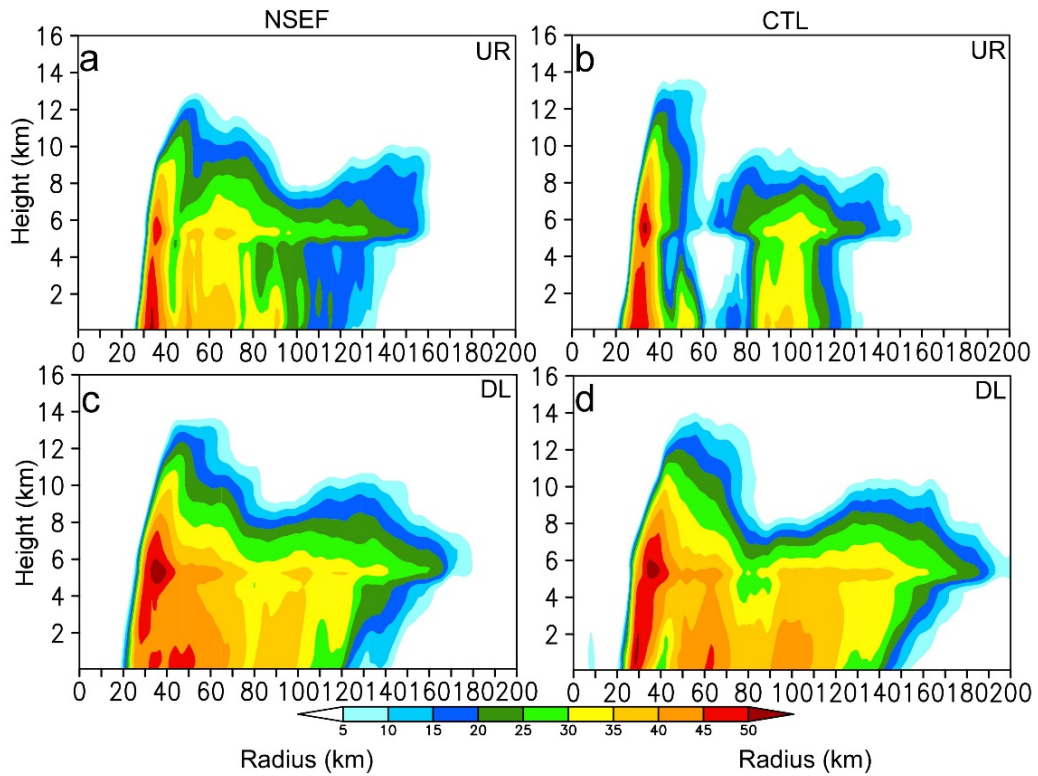


Figure. R1.12 Radius-height cross-sections of the quadrant-mean radar reflectivity (shaded, dBZ) for the (a, b) upshear-right and the (c, d) downshear-left quadrants at 30 h for (a, c) NSEF and (b, d) CTL.

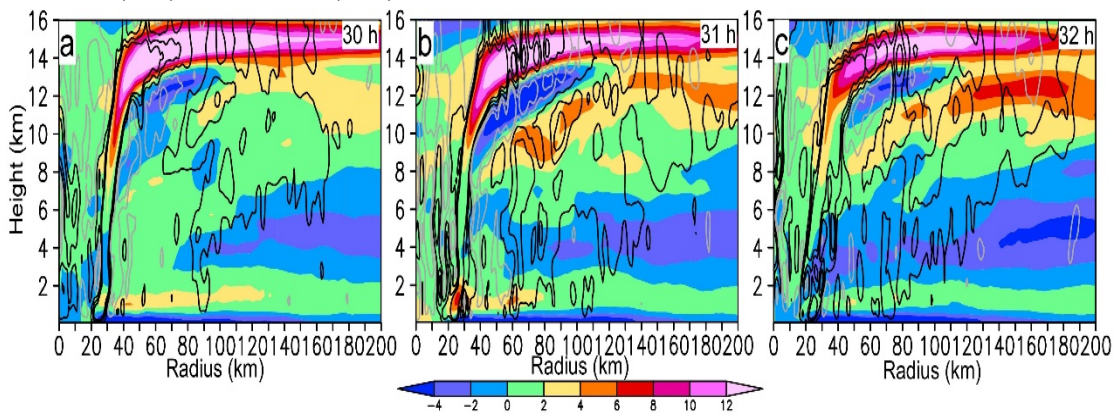


Figure. R1.13 Radius-height cross-sections of the quadrant-mean radial (shaded, m s^{-1}) and vertical wind (black lines of 0.1, 0.3, and 0.5 m s^{-1} ; gray lines of -0.1 and -0.3 m s^{-1}) for the upshear-right quadrant from 30 h to 32 h for CTL.

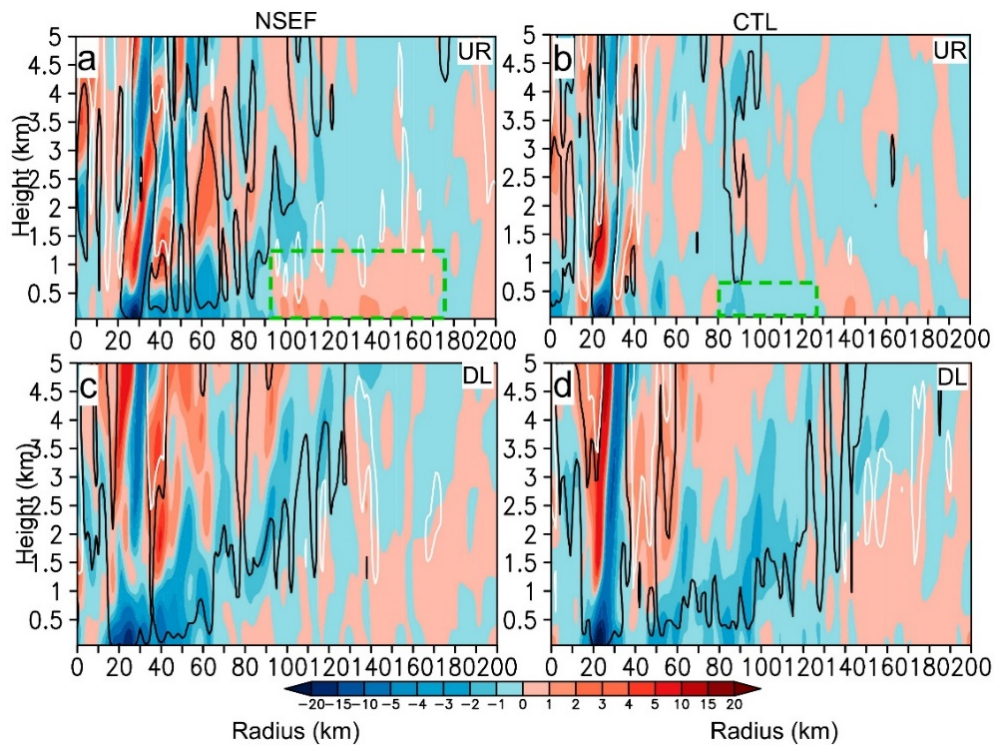


Figure. R1.14 Radius-height cross-sections of the quadrant-mean divergence (shaded, 10^{-4} s^{-1}) superimposed with the vertical wind (black lines of 0.1 m s^{-1} and white lines of -0.1 m s^{-1}) for the (a, b) upshear-right and the (c, d) downshear-left quadrants at 30 h for (a, c) NSEF and (b, d) CTL.

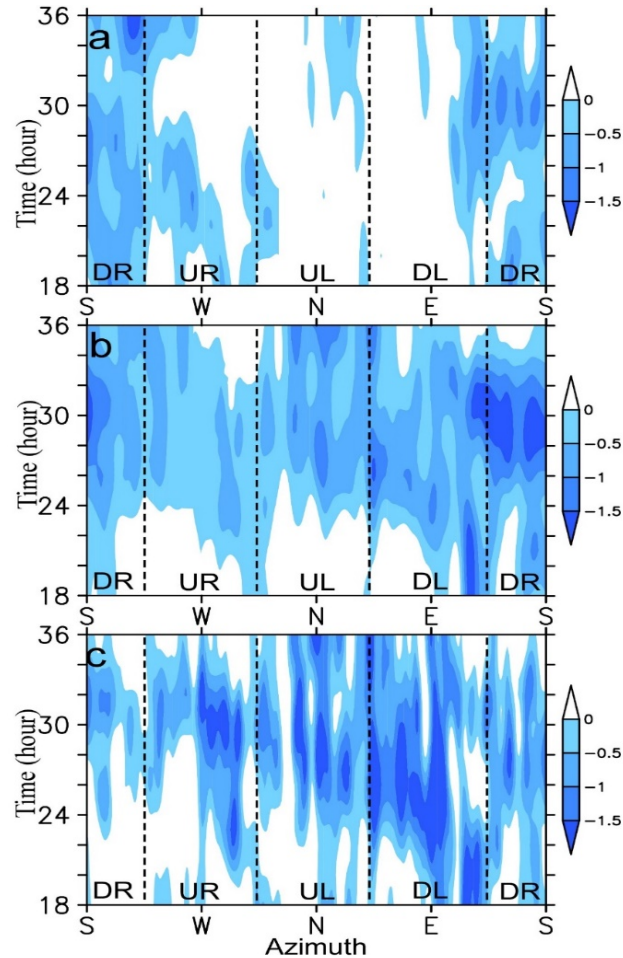


Figure. R1.15 Azimuthal-time cross-sections of the layer-mean (0.05-1.0 km) convergence (shaded, 10^{-4} s^{-1}) averaged from 80-km to 120-km radii of (a) NSEF, (b) CTL, and (c) differences between CTL and NSEF. The black dashed lines indicate the quadrants relative to the large-scale vertical wind shear.

4. There are numerous grammar mistakes in the text. I only list a few. Please carefully edit the text before resubmission.

Replay:

Some passive sentences were changed to positive sentences as you suggested. Some sentences were rewritten. All have been modified in this revision.

Minor comments:

1. Line 25: “The SEF was simulated in the experiment ...” ->” The experiment with ...shows a SEF”.
- Changed.

2. Line 30: “Compared to the simulated . . . , diagnostic analysis”. Rewrite this sentence.
Revised.

3. Line 32: Could the outflow layer itself induce an inflow layer beneath it? A complete Sawyer-Eliassen equation diagnosis is needed.

Thank you for your comment. As shown in our revised Fig. 12, in response to the diabatic warming in the eyewall anvil with large quantities of hydrometeors, an upper-level dry inflow occurs below the anvil. This warming-induced upper-level inflow (almost 50% of the total inflows) is closely associated with the outflow layer under the constraint of the continuity equation.

In the revised manuscript, we emphasized the importance of diabatic heating in the upper-level anvil cloud to the formation of the inflow under the upper-level outflow. The upper-level warming forces radial inflow above the freezing level and this inflow causes a drying effect and promotes diabatic cooling, which is also proposed in Fudeyasu and Wang (2011). The above discussions were added to section 5.3 and the summary in the revision, and the paper by Fudeyasu and Wang (2011) was referred to.

4. Line 58: What is “stretching time”? Probably you mean filamentation time but that needs to be defined too.

It is changed to “*a moderate filamentation time (> 30 min)*”.

5. Line 63: Did Kepert (2013) use an axisymmetric boundary layer model? You may be aware SEF is typically associated with an axisymmetrization of the outer rainband. What insights would you think the axisymmetric framework can provide into this phenomenon?

Yes, Kepert (2013) did use three diagnostic models of the axisymmetric TC boundary layer. The axisymmetric models are limited because they cannot investigate the axisymmetrization of spiral rainbands. This discussion is deleted.

6. Lines 81-82: I agree, and why not focus on this key scientific issue in this study?

Good suggestion. How the spiral rainbands evolve into a closed eyewall is a key issue and has not been fully understood. This manuscript focuses first on the roles of the inner eyewall structure on the moat formation and the SEF when the inner eyewall and the spiral rainband are separated by the moat. Both the moat and the spiral rainband become symmetric during the SEF. The influences of the moat on the evolution of the spiral rainband and the axisymmetrization of the spiral rainband are not discussed in detail in this manuscript, but those will be examined in the future.

7. Line 86: “since” -> due to

Changed.

8. Lines 358-359: I may miss something. Did this study discuss under which situation would upper-level inflows descend into the boundary layer?

You are not missing. This upper-level descending inflow might be not approaching the boundary layer. This upper-level descending inflow enhances the diabatic cooling at middle-to-upper levels, which promotes moat formation.

References:

- Bui, H. H., Smith, R. K., Montgomery, M. T., and Peng, J.: Balanced and unbalanced aspects of tropical cyclone intensification, *Q. J. R. Meteorol. Soc.*, 135, 1715–1731, doi:10.1002/qj.502, 2009.
- Chen X., and Wu, L.: Topographic influence on the motion of tropical cyclones landfalling on the coast of China, *Wea. Forecasting*, 31, 1615-1623, doi: 10.1175/WAF-D-16-0053.1, 2016.
- Dai, Y., Majumdar, S. J., and Nolan, D. S.: The Outflow–Rainband Relationship Induced by Environmental Flow around Tropical Cyclones, *J. Atmos. Sci.*, 76, 1845-1863, doi: 10.1175/JAS-D-18-0208.1, 2019.
- Didlake, A. C., Reasor, P. D., Rogers, R. F., and Lee, W. C.: Dynamics of the transition from Spiral Rainbands to a secondary eyewall in Hurricane Earl (2010), *J. Atmos. Sci.*, 75, 2909-2929, doi: <https://doi.org/10.1175/JAS-D-17-0348.1>, 2018.
- Dodge, P., Burbee, R. W., and Marks, F. D. Jr.: The kinematic structure of a hurricane with sea level pressure less than 900 mb. *Mon. Wea. Rev.*, 127, 987-1004, doi: 10.1175/1520-0493(1999)127<0987:TKSOAH>2.0.CO;2, 1999.

- Duchon, C. E.: Lanczos filtering in one and two dimensions, *J. Appl. Meteor.*, 18, 1016–1022, doi: 10.1175/1520-0450(1979)018<1016:LFIOAT>2.0.CO;2, 1979.
- Fudeyasu, H., and Wang, Y.: Balanced contribution to the intensification of a tropical cyclone simulated in TCM4: Outer-core spinup process, *J. Atmos. Sci.*, 68, 430–449, doi:10.1175/2010JAS3523.1., 2011.
- Kepert, J.: How does the boundary layer contribute to eyewall replacement cycles in axisymmetric tropical cyclones? *J. Atmos. Sci.*, 70, 2808–2830, doi: <https://doi.org/10.1175/JAS-D-13-046.1>, 2013.
- Kossin, J. P., Schubert, W. H., and Montgomery M. T.: Unstable interactions between a hurricane's primary eyewall and a secondary ring of enhanced vorticity, *J. Atmos. Sci.* 57, 3894–3917, doi: [https://doi.org/10.1175/1520-0469\(2001\)058<3893:UIBAHS>2.0.CO;2](https://doi.org/10.1175/1520-0469(2001)058<3893:UIBAHS>2.0.CO;2), 2000.
- Kuo, H.-C., Chang, C.-P., Yang, Y.-T., and Jiang, H.-J.: Western north pacific typhoons with concentric eyewalls, *Mon. Wea. Rev.*, 137, 3758–3770, doi: <https://doi.org/10.1175/2009MWR2850.1>, 2009.
- Montgomery, M.T., Kilroy, G., Smith, R. K. and Črnivec, N.: Contribution of mean and eddy momentum processes to tropical cyclone intensification. *Q. J. R. Meteorol. Soc.*, 146, 3101–3117, <https://doi.org/10.1002/qj.3837>, 2020.
- Rozoff, C. M., Schubert, W. H., and McNoldy B. D.: Rapid filamentation zones in intense tropical cyclones, *J. Atmos. Sci.*, 63, 325–340, doi: 10.1175/JAS3595.1, 2006.
- Terwey, W. D., and Montgomery, M. T.: Secondary eyewall formation in two idealized, full-physics modeled hurricanes, *J. Geophys. Res.*, 113, 1–18, doi: <https://doi.org/10.1029/2007JD008897>, 2008.
- Wang, S., Smith, R. K., and Montgomery, M. T.: Upper-tropospheric inflow layers in tropical cyclones, *Q. J. R. Meteorol. Soc.*, 146, 3466–3487, doi: 10.1002/qj.3856, 2020.
- Wang, Y.: A multiply nested, movable mesh, fully compressible, nonhydrostatic tropical cyclone model-TCM4: Model description and development of asymmetries without explicit asymmetric forcing, *Meteor. Atmos. Phys.*, 97, 93–116, doi: <https://doi.org/10.1007/s00703-006-0246-z>, 2007.
- Wang, Y.: Rapid filamentation zone in a numerically simulated tropical cyclone, *J. Atmos. Sci.*, 65, 1158–1181, doi: 10.1175/2007JAS2426.1, 2008.
- Willoughby, H. E., Clos, J. A., and Shoreibah, M. G.: Concentric eye walls, secondary wind maxima, and the evolution of the hurricane vortex, *J. Atmos. Sci.* 39, 395–411, doi: [https://doi.org/10.1175/1520-0469\(1982\)039<0395:CEWSWM>2.0.CO;2](https://doi.org/10.1175/1520-0469(1982)039<0395:CEWSWM>2.0.CO;2), 1982.
- Wu L., and Chen, X.: Revisiting the steering principal of tropical cyclone motion, *Atmos. Chem. Phys.* 16, 14925–14936, doi: <https://doi.org/10.5194/acp-16-14925-2016>, 2016.
- Zhu, Z., and Zhu, P.: The role of outer rainband convection in governing the eyewall replacement cycle in numerical simulations of tropical cyclones, *J. Geophys. Res. Atmos.*, 119, 8049–8072, doi: 10.1002/2014JD021899, 2014.
- Zhu Z., and Zhu, P.: Sensitivities of eyewall replacement cycle to model physics, vortex

structure, and background winds in numerical simulations of tropical cyclones, *J. Geophys. Res. Atmos.*, 120, 590-622, doi: doi:10.1002/2015GL066436., 2015.